SANDIA REPORT
SAND2020-5210
Printed May 2020

Sandia National Laboratories

Evaluating MetGlas™ Solderability with Tin-Silver-Copper and Tin-Silver-Bismuth Solder Alloys

Rebecca A. Wheeling, Paul T. Vianco, Shelley M. Williams

Prepared by
Sandia National Laboratories
Albuquerque, New Mexico
87185 and Livermore,
California 94550

Issued by Sandia National Laboratories, operated for the United States Department of Energy by National Technology & Engineering Solutions of Sandia, LLC.

Available to DOE and DOE contractors from
U.S. Department of Energy
Office of Scientific and Technical Information
P.O. Box 62
Oak Ridge, TN 37831

Telephone: (865) 576-8401
Facsimile: (865) 576-5728
E-Mail: reports@osti.gov
Online ordering: http://www.osti.gov/scitech

Available to the public from
U.S. Department of Commerce
National Technical Information Service
5301 Shawnee Rd
Alexandria, VA 22312

Telephone: (800) 553-6847
Facsimile: (703) 605-6900
E-Mail: orders@ntis.gov
Online order: https://classic.ntis.gov/help/order-methods/

ABSTRACT

The solderability of MetGlas™ (subsidiary of Hitachi Metals, America Ltd) 2826 MB, a rapidly solidified metallic foil, was evaluated by the meniscus height/wetting force method for tin-silver-copper (SnAgCu) and tin-silver-bismuth (SnAgBi) solders to understand the effects of the extreme non-equilibrium condition of the Metglas™ surface on solderability performance. Of the variables studied here (solder temperature, heat treatment, and solder composition), solder composition had the largest impact on contact angle. Flux and foil composition remained constant throughout; but, these factors would also be predicted to significantly affect solderability. A greater understanding of the manner whereby non-equilibrium cooling affects solderability of these foils will broaden the application of soldering technology of structures fabricated by rapid cooling process (i.e. additively manufactured coatings and parts). Developing a robust database for Pb-free solderability behavior is also necessary, as industry transitions from tin-lead (SnPb) to lead free (Pb-free) solders.

ACKNOWLEDGEMENTS

Authors would like to acknowledge Sandia's *Aging and Lifetime Program*, for providing funding for this work.

CONTENTS

LIST OF FIGURES

LIST OF TABLES

This page left blank

ACRONYMS AND DEFINITIONS

Abbreviation	Definition
SnAgCu	tin-silver-copper solder (also referred to as SAC alloys, though not in this paper)
SnAgBi	tin-silver-bismuth solder
SnPb	tin-lead solder
IMC	intermetallic compound

1. INTRODUCTION

1.1. Solderability

Forming satisfactory solder joints requires, among other considerations, molten solder to wet and spread along the faying surface areas [1]. *Solderability* is defined as the capacity for the solder system to support wetting and spreading by the molten solder towards formation of a solder joint [2]. A solder system is comprised of the solder material, flux chemistry, and base/substrate material(s). Controlled atmospheres may be used in place of, or in combination with, the flux. "Good" solderability implies a high propensity for producing a sound solder joint since the molten solder will flow to completely fill the joint gap and form an adequate fillet. In the case of base materials, key factors include composition, topology, oxides, and extraneous contaminants that affect wetting and spreading activity. But, it is difficult to visually differentiate surfaces having "satisfactory" or only marginal-wettability surfaces from those having "good," wetting. An alternative, quantitative means is necessary to assess solderability [1]. Solderability testing and, specifically, the meniscus height/wetting force method, offers an avenue to quantitatively assess solder wetting and spreading on the base material surfaces using the appropriate filler metals, fluxes, and process temperatures.

1.2. Evaluating Solderability

Solderability testing provides a first-order insight into a soldering process by examining the materials set used in the soldering system within a controlled, laboratory environment. Evaluating wetting and spreading is critical towards the selection of the base material, the solder alloy (filler metal), the flux, and the solder processing parameters. As new materials are designed, engineered, and put into service, it is important to evaluate their solderability early in the design process to determine if soldering is a viable joining option. If several base materials, filler metals, or fluxes are being considered for a given application, solderability testing provides a comparative tool for down-selecting the appropriate system. During manufacturing, a base substrate and solder alloy should have already been appropriately chosen and deemed adequate for the application. However, soldering may not occur immediately in the fabrication process, and substrate storage and aging may affect the originally acceptable solderability. By aging test specimens to reflect manufacturing conditions or by using actual, stored parts, solderability testing can be used to identify changes in solderability imparted by environmental and/or aging effects [2, 3].

Solderability testing provides a first-order assessment tool. However, such testing may not correlate directly with wetting and spreading in an actual joint geometry or soldering process. Capillary effects (due to part spacing), heating profile, and even environmental effects cannot be entirely taken into account within the scope of a laboratory solderability test. Also, solderability tests introduce a small base material coupon into a relatively large pot of molten solder. More solder is available during solderability testing than would be made available in an actual joint, which poses additional surface tension effects. In addition, large volumes of liquid solder can promote faster surface dissolution rates than would occur during a soldering operation for comparable times and temperatures [1]. In solder joints, the solder may experience more temperature variation, thereby promoting different metallurgical reactions between the liquid solder and the metal substrate [1]. Metallurgical reactions can induce surface tension changes that alter the wetting and spreading driving forces *in real time*. Of course, other physical and mechanical factors, which include processing conditions, joint design, and service conditions, must be considered when designing and developing successful solder joints. Although solderability testing cannot consider all of the factors relevant to the soldering of a joint, it does provide a first-order assessment with which to compare the wetting and spreading performance of base material/filler metal/flux systems.

In general, solderability tests are separated into two groups: visual inspection (qualitative) criteria and quantitative measurements [2]. Time, temperature, solder composition, and flux can be varied to understand their respective effects on solder wetting and spreading using either approach [1].

1.2.1. Visual Inspection

"Visual Inspection Criteria" are qualitative and generally expressed as a pass/fail outcome. Common visual solderability tests include *Dip and Look (DNL)*, *Wrapped Wires*, *Surface Mount Process Simulation (SMT)*, and others [3]. The DNL test is generally regarded as the most straightforward procedure and is routinely used for testing integrated circuit device leads and other input/output (I/O) configurations on electronic packages [1]. Leads are immersed in an appropriate flux, then dipped into molten solder for 5-10 s. The percentage of the lead surface that remains unwetted is visually determined, with most standards specifying that "all terminations shall exhibit a continuous solder coating, free from defects for a minimum of 95% of the critical surface area of any individual termination" [1]. Details regarding these tests are available in relevant industry standards [3-5]. The objective of these tests is to apply a less subjective, albeit still qualitative assessment to the aforementioned designations: "good," "bad," and "marginal". However, they do not provide information regarding in-situ dynamics of wetting and spreading behavior [2, 3].

1.2.2. Quantitative Assessment

Quantitative solderability testing involves dipping a specimen coupon into a molten solder pot while concurrently measuring the meniscus weight as a function of time using the *wetting balance* instrument. The meniscus weight, which is the resolved vertical force (F_R) acting on the specimen, is shown as a function of time in Figure 1-1 [1]. The initial non-wetting behavior results in a force in the upward direction and is shown on the negative scale. Wetting, which creates the meniscus weight, results in a downward force and is shown on the positive scale [6]. Buoyancy forces (F_B), which are negative, are taken into account when analyzing the test results. Figure 1 illustrates a force diagram for a sample during dipping and a schematic force-time curve over the course of one dipping cycle.

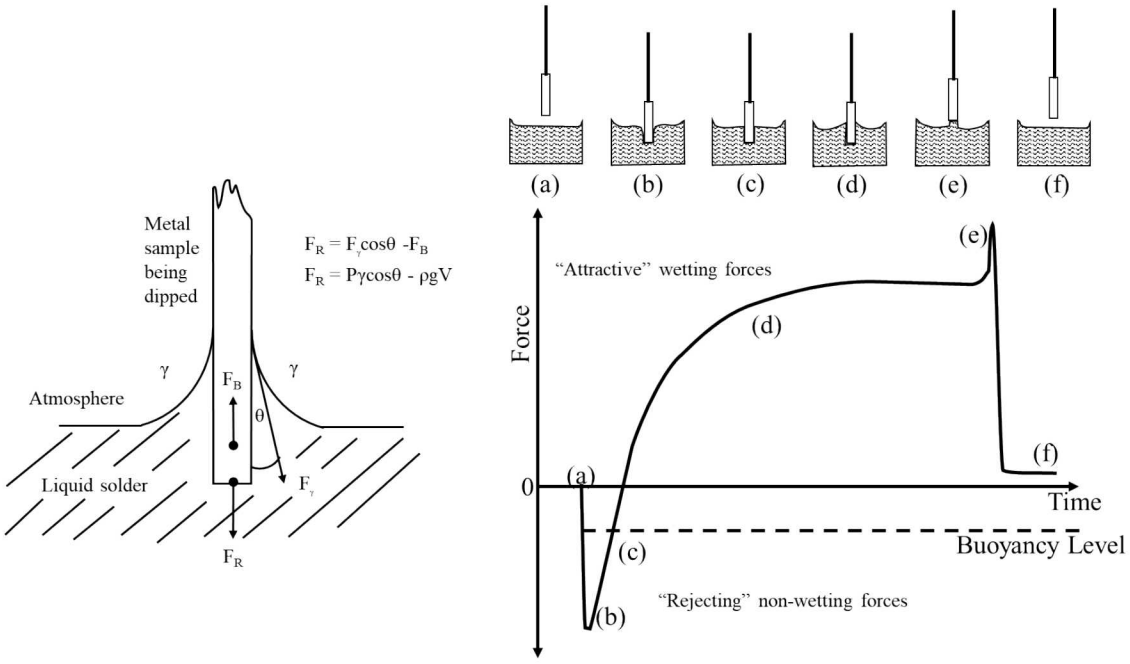

Figure 1-1. Force diagram schematic for a solid coupon dipped into a liquid (left), adapted from Humpston; Schematic wetting balance curve with corresponding regions for various points in a dip cycle (right), adapted from Xu, et al. [1, 6]. P (specimen periphery length), γ (liquid surface tension), θ (contact angle), ρ (liquid density), g (gravitational constant, 9.81 m^2/s), V (immersed volume).

The wetting process is described with reference to the illustrations in Fig. 1-1. Prior to dipping, the liquid imparts no force on the test coupon (a). As the coupon is lowered into the molten solder, the test coupon displaces liquid, and the latter exerts an upward buoyancy force on the test coupon (b). No wetting has occurred, as yet. Wassink suggested that this initial delay results from the time it takes for the substrate temperature to reach the bath temperature [7]. A second, contributing factor is the time required for the flux to activate. The upward force exerted by the liquid is determined by the volume of the submerged coupon plus the volume of the negative meniscus. The buoyancy force is used to shift the x-axis in order to make relative comparisons of wetting between different materials. When wetting initiates, the initial upward force reverses as the molten solder meniscus begins to "pull" down on the coupon (between b and c). This downward force increases as the solder wets further up the coupon faces (c-d). When wetting ceases, the downward force reaches a peak value between (d) and (e). Upon removal of the coupon from the liquid solder, an increased downward force is realized as the meniscus is pulled upwards for a moment (e) which then quickly drops back to zero (f) upon release of the meniscus. Most reported wetting curves do not include the sample removal segment since that data is not relevant to the solderability analysis..

Curve shapes and curve-specific metrics like *Time to Zero Force* (t_0), *Time to Two-Thirds Maximum Force* ($t_{2/3}$), *Time to Maximum Force* (t_{Max}), *Maximum Force* (F_{Max}), and wetting rate can be used to further evaluate solderability. Figure 1-2 illustrates the potential range of wetting curves based upon differences in F_{max} and $t_{2/3}$.

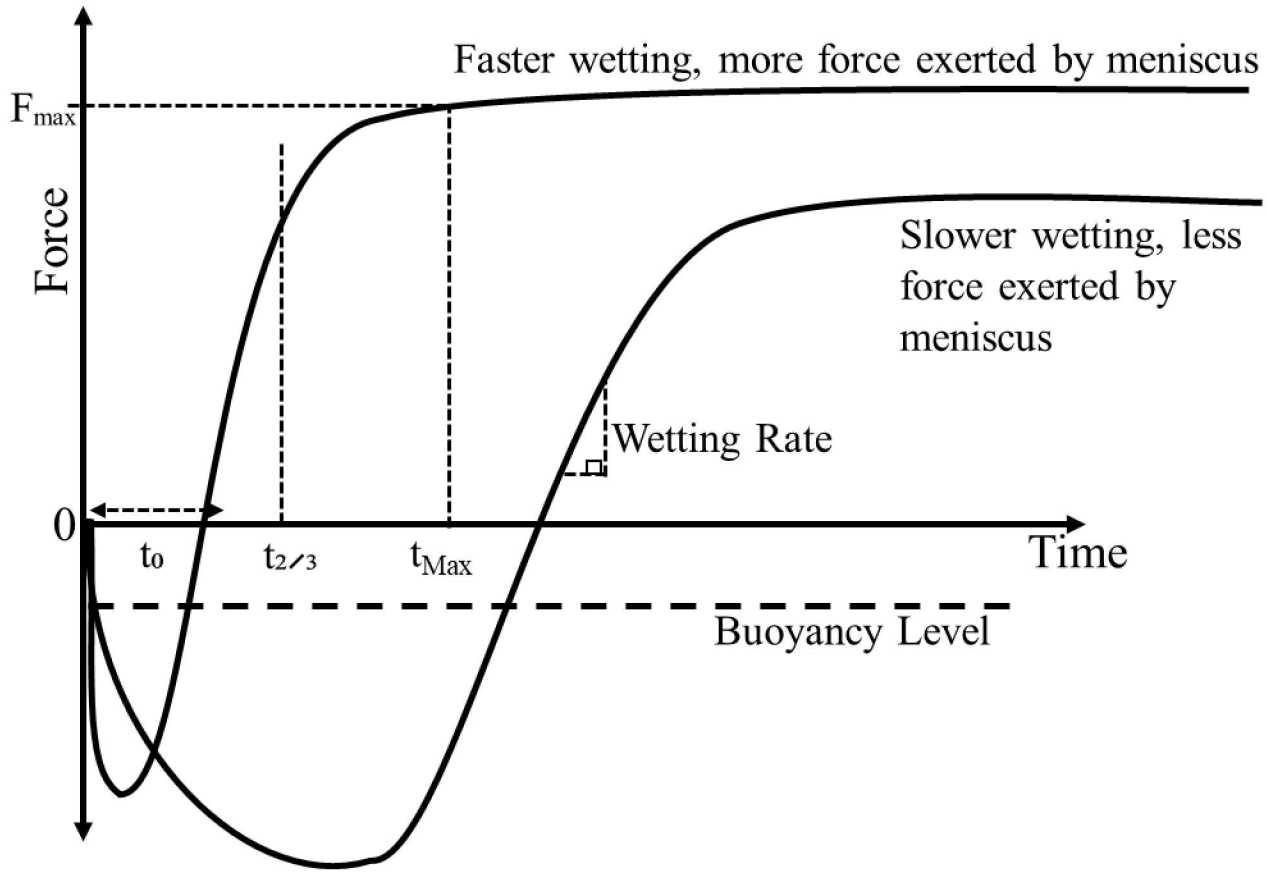

Figure 1-2. Schematic illustrating the differences in wetting performances that wetting curves can capture.

"Good" solderability is indicated for solder/flux/substrate systems by low t_0, $t_{2/3}$, and t_{Max} values in conjunction with high F_{Max} and wetting rate values. A low t_0 value indicates that wetting initiates very soon after dipping, and the nearer $t_{2/3}$ and t_{Max} are to t_0, the faster the wetting rate as the molten solder travels along the coupon surface. Figure 1-3 illustrates how wetting curve shape correlates to various wetting behaviors.

A high F_{Max} value indicates the magnitude of the solderability for that solder/flux/substrate system. However, F_{Max} depends on the *shape* of the meniscus so that a small value of F_{Max} does not necessarily indicate a reduced solderability performance. Therefore, it is necessary to use the contact angle to describe the relative solderability performances between different solder/flux/substrate systems in order to eliminate this ambiguity. *Lower the contact angle value, better is the solderability.* Quantitative solderability test methods are valuable for obtaining "pristine," laboratory. If solderability is poor in these tests, the performance is unlikely to improve in an actual application. [1, 3, 8] On the other hand, when good solderability is indicated by these laboratory evaluations, a significant potential exists for good solderability in the industry process.

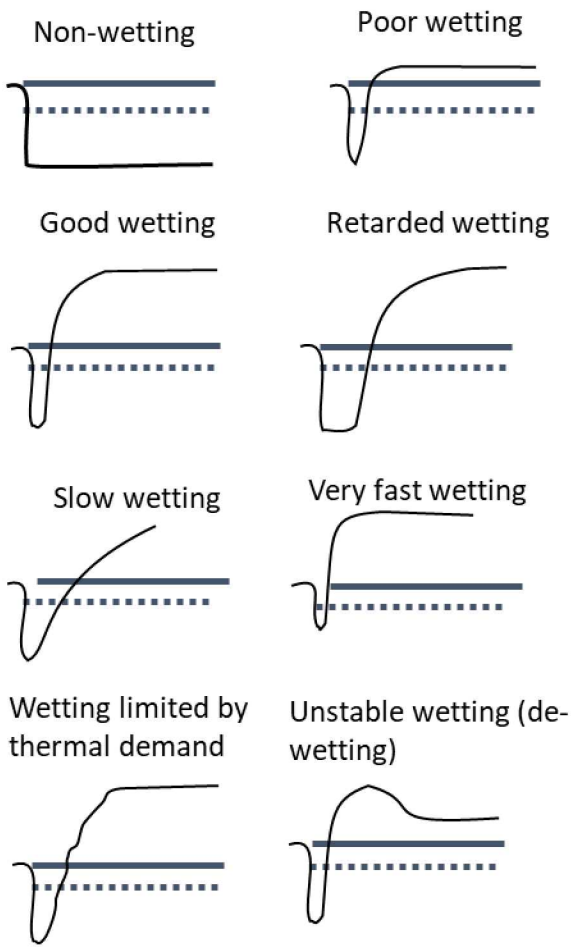

Figure 1-3. Schematic illustrations of various wetting curve shapes and their correlation to solderability behavior.

Of course, different overall curves can exhibit similar values of t_0, $t_{2/3}$, t_{Max}, wetting rate and/or F_{max}., Other than contact angle, these metrics cannot singly compare solderability between different solder/flux/substrate systems. Also, there is not necessarily a direct correlation between each of the metrics. For example, five different materials with different solderability tendencies may all exhibit identical t_0 values, but the wetting rates may differ, significantly. Claiming that all five would exhibit similar solderability based only on t_o would not accurate. An improved approach is to consider the above metrics to complementary of each other so that a thorough analysis must evaluate *all* of the parameters. Lastly, the wetting balance test can be complemented with other solderability testing methodologies described in the literature [9, 10]. For example, contact angle measurements can be obtained by enhanced sessile drop test [11].

1.3. Metallic Glass

This study utilized wetting balance testing and associated analyses to evaluate the solderability of two Pb-free solder alloys: 96.5Sn-3.0Ag-0.5Cu (wt.%) and 91.84Sn-3.33Ag-4.83Bi, abbreviated SnAgCu and SnAgBi, respectively. The base material was the metallic glass alloy, (40 – 50)Fe-(40-50)Ni-(5-10)Mo-(1-5)B having the tradename, MetGlas™ 2826MB (Metglas, Inc., Conway, SC).

A brief review is given of metallic glasses. Metallic glasses are used commercially in low loss transformer core, magnetic shielding, and sensor applications [12]. The 2826 MB alloy is specifically used for magnetoelastic sensor applications [13]. Metallic glasses have amorphous metal structures that result from the molten material being quenched with cooling rates on the order of 1E6 °C/s. During such rapid solidification, the atomic disorder from the liquid state is preserved because the short time does not allow for atomic arrangement into ordered, crystalline structures. These rapid cooling rates are realized in a "melt spinning" method where molten metal streams onto a spinning wheel, solidifies, and produces a thin, foil-like ribbon of metallic glass as illustrated by Figure 1-4 [12].

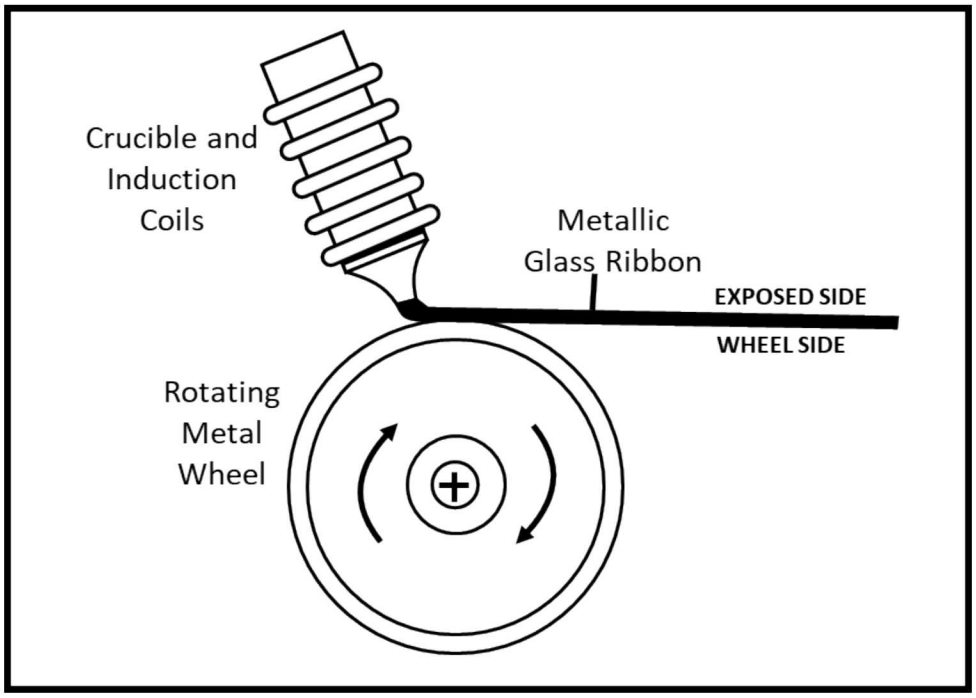

Figure 1-4. Schematic of the spinning process used to cast metallic glass foils, adapted from Vianco, et al. [12].

Different surface conditions are observed for the front and back sides of the ribbon, which correspond to the "exposed" and "wheel" sides, respectively. The back surface that experiences wheel contact during cooling is shiny in contrast to the dull, front side that cools in contact with air. Figure 1-5 illustrates the difference between the 2 sides. The ribbon thickness is very important, as cooling rates decrease with increasing thickness. Thicknesses less than 0.01 cm (0.004 in) are associated with sufficiently-fast enough cooling rates to form the metallic glass.

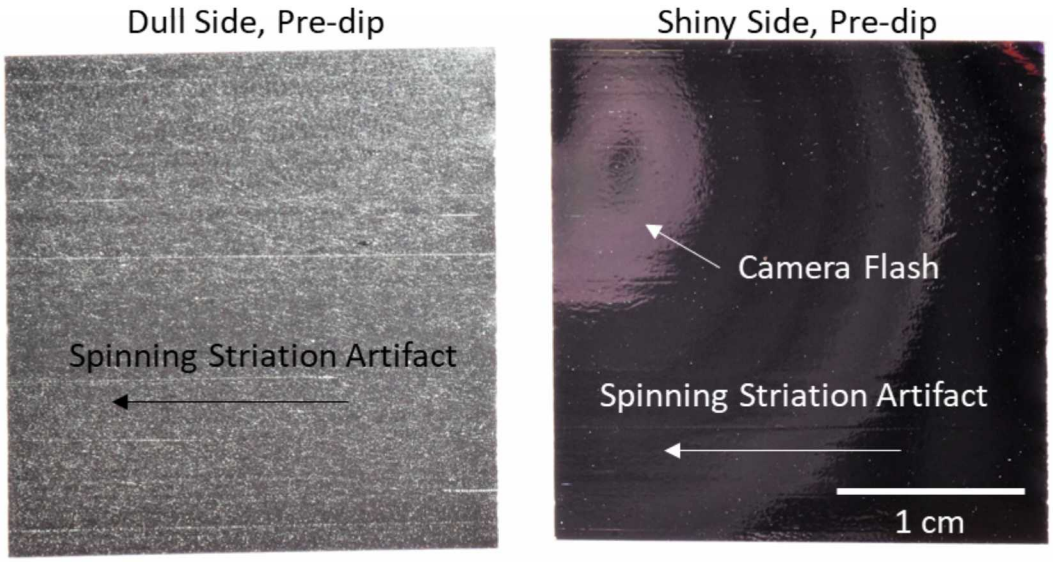

Figure 1-5. The dull, "exposed" side and the shiny, "wheel" sides of a given MetGlas™ coupon.

Joining metallic glasses is problematic due to the metastable, amorphous atomic structure that will begin to order when exposed to elevated temperatures. This process is referred to as *structural relaxation*. At sufficiently high temperatures, complete crystallization can occur, eliminating the unique material properties imparted by the disordered structure. Such temperature considerations limit joining metallic glasses to low temperature methods like fastening and soldering. Vianco et al. recognized the need for a technical understanding of metallic glass joining and evaluated the solderability of several metallic glass compositions as functions of solder alloy, flux, and surface preparation [12]. They also noted how wettability was significantly reduced as the amorphous structure began to order, that is, undergo structural relaxation.

In the present study, the solderability of an Fe-Ni metallic glass substrate was evaluated with the two, aforementioned Pb-free solders, SnAgCu and SnAgBi. Five (5) aging conditions were imposed on the samples to better understand structural relaxation effects regarding solderability.

2. EXPERIMENTAL PROCEDURE

2.1. Wetting Balance

A wetting balance was utilized to assess the solderability of MetGlas™ 2826 MB with two Pb-free solder compositions: 96.5Sn-3.0Ag-0.5Cu (wt.%, designated SAC 305) and 91.84Sn-3.33Ag-4.83Bi (Sn-Ag-Bi). The nominal composition (wt. %) of MetGlas™ 2826 MB is 40-50Fe-40-50Ni-5-10Mo-1-5B, and up to 0.3 wt.% Co as a trace impurity. Coupons were fabricated with the dimensions of 2.54 x 2.54 x 0.05 cm and were evaluated after exposure to one of the following five aging treatments: as-received (baseline); aged at 100 °C (for 4 and 8 hrs); and aged at 250 °C (for 4 and 8 hrs). All heat-treatments occurred under vacuum conditions. Figure 2-1 depicts the testing matrix. Immediately prior to solderability testing, all coupons were rinsed ultrasonically in the degreasing solvent, trichloroethylene (TCE) and subsequently in isopropanol (IPA) and dried in flowing nitrogen before applying *Stay Clean® Aluminum Flux* (SCAF-4). Testing occurred with solder pot temperatures of 240 and 260 °C. Coupons were dipped 0.4 cm into the molten solder at a rate of 5.0 mm/s, held for 10.0 s, and lastly raised from the solder at a rate of 10.0 mm/s. Immediately after testing, coupons were cleaned using the same pre-dip cleaning procedure.

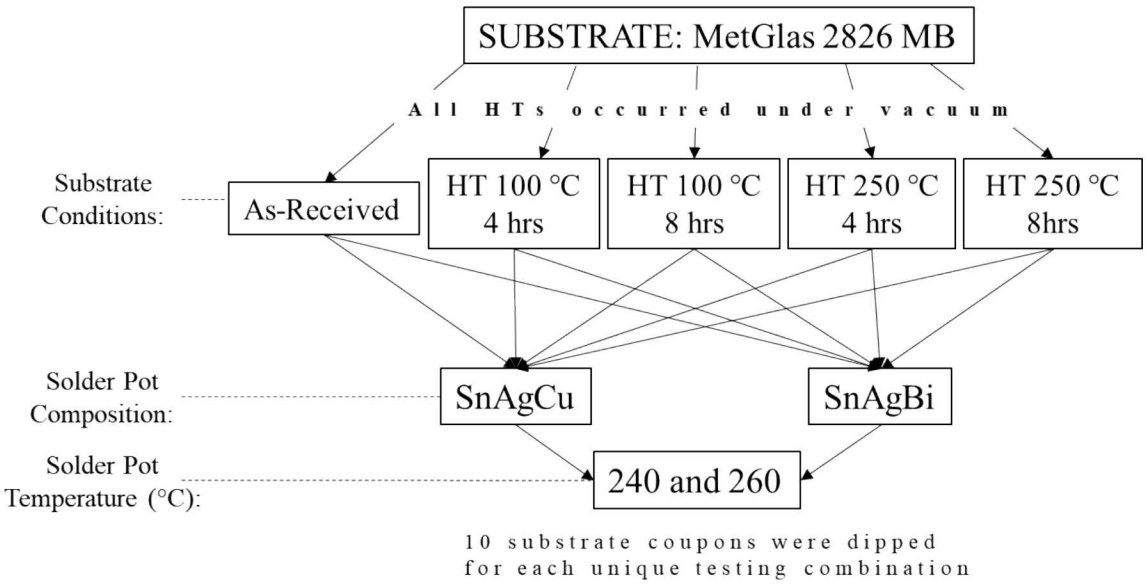

Figure 2-1. The varied heat treatment conditions, solder compositions, and testing temperatures for the MetGlas wetting balance test scheme.

2.2. Wettability Metrics

Quantitative and qualitative evaluations followed the immersion of each coupon. The wetting balance technique allowed for the experimental measurement of the meniscus height and weight, from which these parameters could be determined: contact angle, solder-flux interfacial tension, wetting rate, and wetting time. Meniscus heights were measured, manually, after the solderability test. The meniscus weight values were measured in situ by the wetting balance apparatus. In addition, a post-dip solder assessment provided qualitative interpretation of solderability, including the occurrence of non-wetting and dewetting behaviors.

2.2.1. Meniscus Height and Weight

Figure 2-2 illustrates the meniscus height measurement after the solderability test. All coupons were oriented with the casting striations parallel to the solder surface, as it has been shown that the surface striation orientation can effect meniscus rise behavior [12]. Differences between meniscus heights on the "wheel" relative to the "exposed" sides were also assessed, separately.

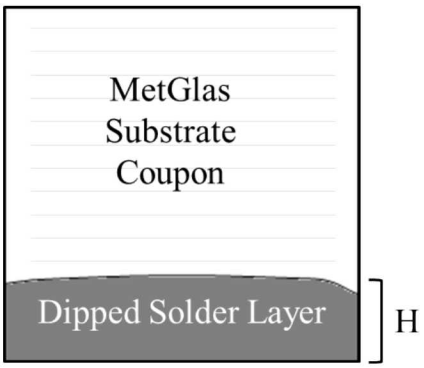

Figure 2-2. Schematic of a dipped coupon, where the meniscus height measurement is H.

Meniscus weight is measured in situ (as the weight exerted of the solder meniscus) by the wetting balance.. This meniscus weight value, per coupon, is an average of the weights from both sample sides.

2.2.2. Wetting Rate

Once wetting initiates, liquid solder continues to travel up the coupon surface at nearly a constant rate. The wetting rate diminishes as the meniscus reaches its maximum height.

2.2.3. Contact Angle

Contact angles, θ_{C1} and θ_{C2}, were calculated for the "wheel" and "exposed" sides, respectively, using Equation 1:

$$\theta_{Ci} = sin^{-1}(1 - \frac{\rho g H_i^2}{2\gamma_{LF}}) \quad (1)$$

$\theta_{C,i}$ - Contact Angle (°)

ϱ ---- Solder density (g/cm^3)

g ---- Acceleration due to gravity (cm/s^2)

H_i --- Meniscus height (cm)

γ_{LF} --- Solder-flux surface tension (dynes/cm)

Contact angles are the preferred measure of solderability because they reflect a resultant interaction between the three interfacial tensions (related through Young's equation) present during liquid wetting of a solid substrate, as shown in Figure 2-3.

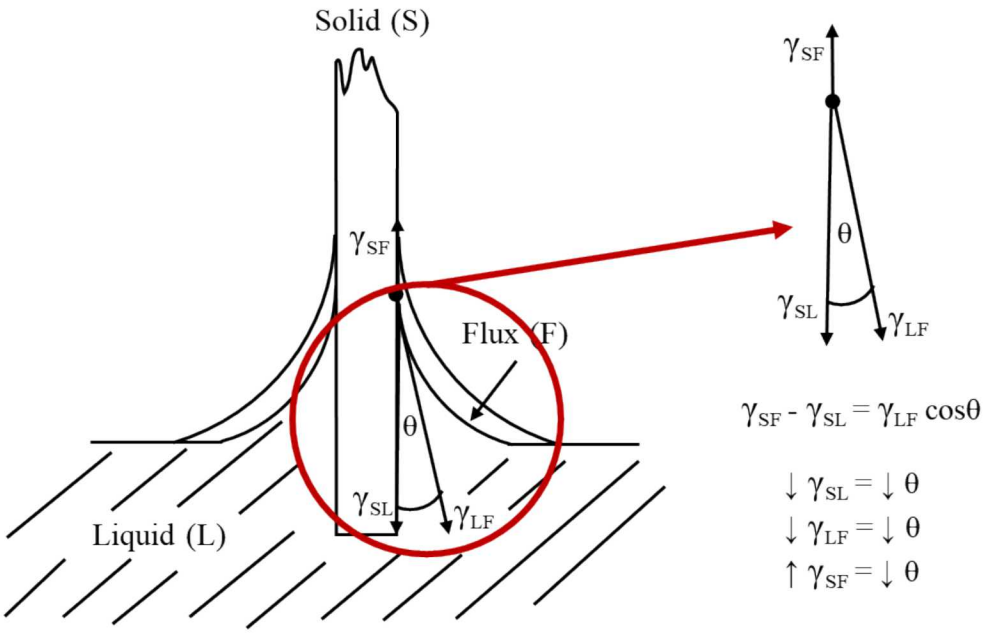

Figure 2-3. Interactions between solid-flux (SF), solid-liquid (SL), and liquid-flux (LF) interfacial tensions when a solid is coated with a flux and dipped into molten solder (left). The relationship between these interfacial tensions as defined by Young's equation is shown on the right.

The lower the contact angle, the better is the solderability. Contact angle is minimized when the solid-liquid and liquid-flux interfacial (surface) tensions are minimized, and the solid-flux interfacial tension is at a maximum. Conceptually, this trend makes sense: if the solid-flux interfacial energy is the highest of the three, it is also the "least preferred" condition because the systems as a whole wants to "move" toward the lowest free energy, which is also the most stable configuration. In this case, the "system" refers to the combination of coupon, flux, and molten solder. If the solid-flux interfacial energy is lower than the other two, there will be no driving force for the liquid solder to displace the flux and wet the solid substrate because the interfacial energy would not decrease upon doing so; therefore, fluxes must reduce their interfacial tensions with liquid solder to promote solderability. Lower solid-liquid and liquid-flux interfacial energies create a scenario in which liquid solder wets and spreads, thereby replacing the higher energy solid-flux interface with the lower energy, more preferred solid-liquid interface.

In practice, the solid-liquid interfacial energy, γ_{SL}, is minimized with proper solder alloy and substrate material selections, which determine the interface reaction between the two materials. That reaction is typically the formation of an intermetallic compound (IMC). The liquid-flux interfacial energy, γ_{LF}, is minimized during flux activation. Finally, the solid-flux interfacial energy, γ_{SF}, is maximized with surface cleanliness, surface oxide removal, and substrate material selection. Table 1 shows the generally accepted wetting trends associated with contact angles [14].

Table 1-1. Wetting behavior categories associated with contact angle ranges.

Contact Angle (º)	Wetting Behavior
0-10	Perfect
10-20	Excellent
20-30	Very Good

Contact Angle (º)	Wetting Behavior
30-40	Good
40-55	Adequate
55-70	Poor to Fair
70-90	Very Poor
90+	No Wetting

If meniscus height values vary significantly between the "wheel" and "exposed" sides, the coupon experiences non-symmetrical forces from asymmetrical menisci, resulting in a net sample tilt as illustrated in Figure 2-4. A significant tilt would cause a discrepancy between the actual contact angles and those calculated with Equation 1.

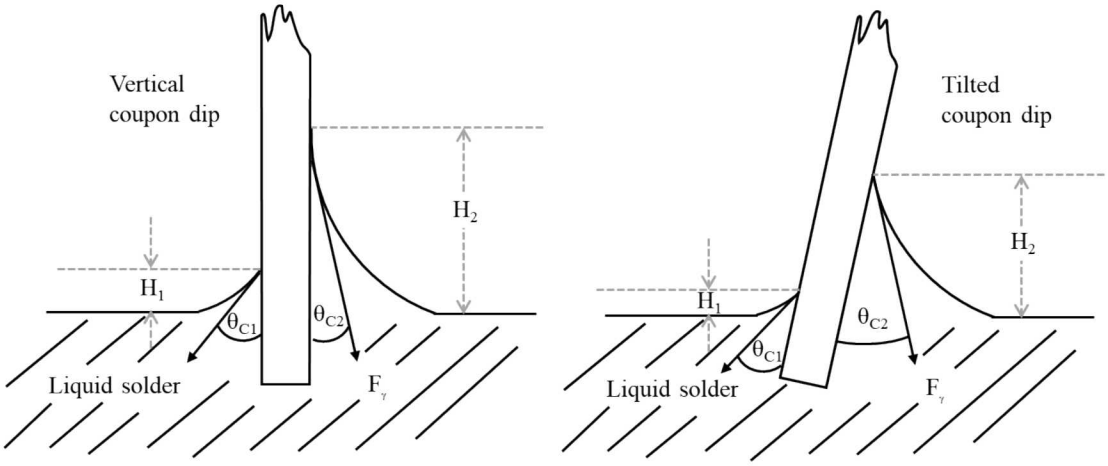

Figure 2-4. An ideal, vertical coupon dip (left) where the correct contact angles can be calculated, and a tiled coupon dip (right) where the calculated contact angles would not represent the actual contact angles.

Vianco took asymmetric sample tilting into account in order to verify the integrity of the wettability data when testing MetGlas™ coupons. Slight wetting variations between the "wheel" and "exposed" sides were recorded; however, the differences were within the experimental error and as such, did not significantly impact the contact angle determinations.[12]. Due to the similarities between Vianco's previous study and the current study, that prior finding was assumed to be applicable to the present data. The calculations used by Vianco to calculate tilt angles for a given sample are provided in Appendix A.

2.2.4. Solder-Flux (Liquid-Flux) Interfacial Energy

While contact angle values reflect the interaction between the three interfacial energies, it is also useful to assess each individual interfacial energy; however, only the solder-flux interfacial energy can be calculated from the test data. Though the flux remained constant throughout the study, the solder-flux interface energy can potentially differ between the two solder compositions. The solder-flux interfacial tensions were calculated and reported to understand their impact on the overall solderability behavior. It was expected that the solder-flux interfacial energies would exhibit a bimodal distribution stemming from the two solder compositions. Other significant interfacial

energy changes within each of the two solder sample sets would be at the solid-solder and solid-flux interfaces due to any structural surface changes attributed to potential relaxation and short-term ordering of the MetGlas substrates; however, these values cannot be calculated from this test procedure. As such, surface structure effects on wettability can only be qualitatively inferred. Even so, the solder-flux interfacial tensions still provide information regarding each liquid solder's interactions with the flux. The calculation derivation can be found in Appendix A.

2.2.5. Force vs. Time Curves

The ten wetting curves for each condition were averaged and compared to evaluate obvious qualitative differences.

2.2.6. Solder Assessment

The continuity of solder coating that solidified on the MetGlas™ coupons was evaluated after dipping. A continuous solder coating constitutes "good"/ideal solderability, where a metallurgical bond formed at the solder/MetGlas™ interface. "Non-wetting" and/or "de-wetting" reflect poor solderability. Non-wetting occurs if a metallurgical bond is not established, i.e. when an interface reaction, including interdiffusion, has not taken place. De-wetting occurs if incomplete intermetallic layers form, hence "driving" most of the available liquid to the regions adjacent the intermetallic layer. Bare or oxidized substrate material remains after the liquid recedes. Clearly, this scenario is undesirable for solder joint performance and reliability. Figure 2-5 illustrates solder wetting compared to non-wetting and de-wetting.

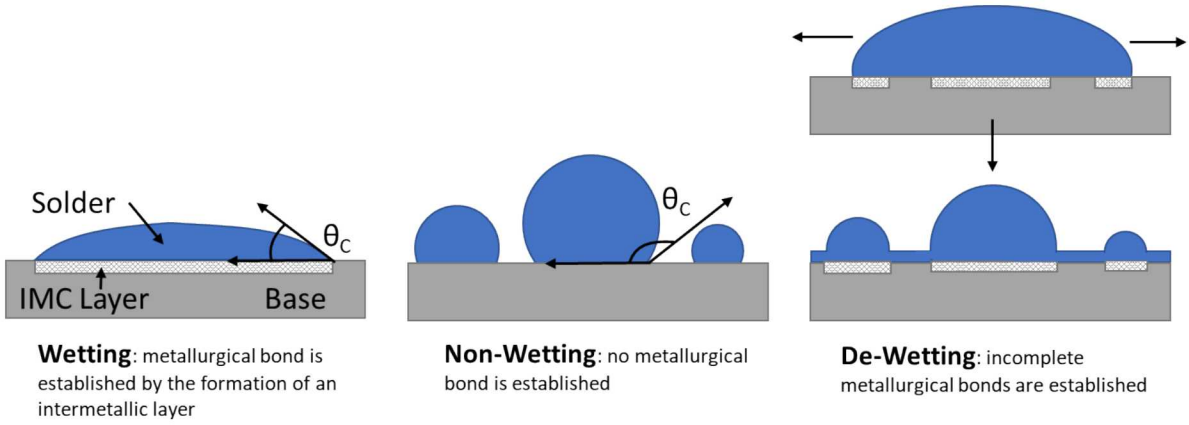

Figure 2-5. Schematic, cross-section illustration of the three wetting conditions: wetting, non-wetting, and de-wetting [15, 16]

3. RESULTS & DISCUSSION

3.1. Meniscus Height and Weight

Figure 3-1 shows the measured meniscus height values for the entirety of the experiment. The measurements are divided by aging condition. The exposed vs. wheel side measurements are plotted separately. The colors denote solder and solder temperature.

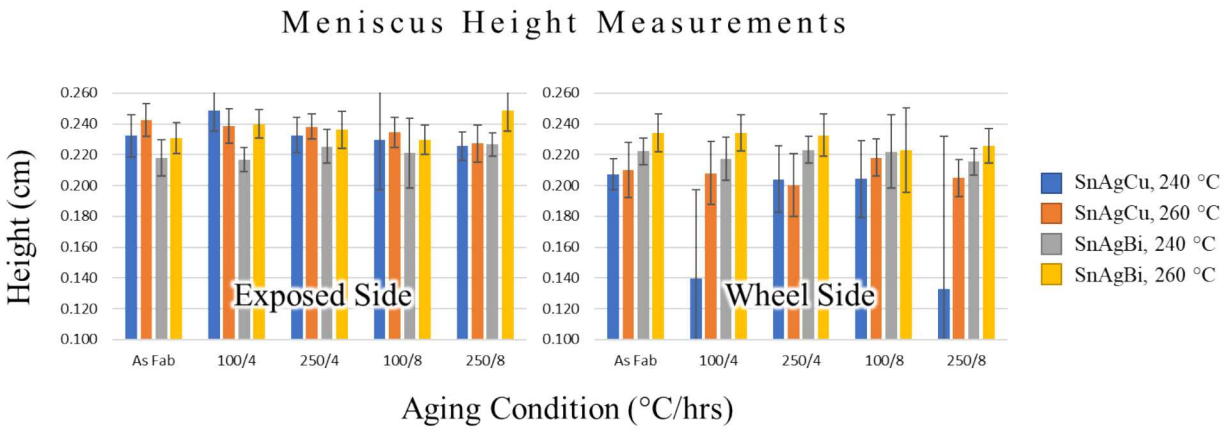

Figure 3-1. Meniscus height values for SnAgCu or SnAgBi solder are shown as a function of coupon aging conditions as well as solder temperature. Error bars reflect standard deviations of the data sets.

Most meniscus heights were between 0.20 and 0.25 cm. The SnAgBi solder exhibited similar meniscal heights on both sides while the SnAgCu exhibited generally lower *mean* heights on the wheel side, but still statistically the same as those on the exposed side to within the error bars. Comparing the wheel side data to the exposed side findings, the differences of mean values were greater between each sample set in the former case as was also, a larger degree of scatter observed in the wheel side results. The lower meniscal heights on the wheel side could reflect different surface conditions. Surface topology/morphology are different between the two sides. The side that solidified on the wheel was much smoother than the exposed side. Composition and/or atomic structural difference – e.g., degree of disorder could also exist between the two sides if a thermal gradient (from wheel to exposed side) existed during cooling. The wheel side would experience faster cooling rates. It may be possible that a higher degree of disorder was present on the wheel side, creating a larger driving force to re-order/crystallize over time (to minimize energy). An altering of the chemical potential would, in turn, change its reaction with the molten solder vis-à-vis the exposed side. Different dissolution behavior of the base material into the solder may impact the interfacial energy relationships, in this case increasing the interfacial energy on the wheel side (reducing solderability). Different thicknesses of the intermetallic compound (IMC) layer would indicate different reaction thermodynamics between the two sides. Confirming measurements would require x-ray or transmission electron microscope (TEM) analyses to determine the extent of disorder as well as Auger electron spectroscopy (AES) and x-ray photoelectron spectroscopy (XPS) to confirm the surface chemical composition, all of which were beyond the scope of this study..

The SnAgBi solder produced higher meniscus heights (regardless of solder temperature) for all aging conditions. The following two sample sets, which originated from the wheel side, produced significantly lower meniscus heights: SnAgCu/240 °C; following aging at 100 °C for 4 hours and the

same solder and temperature after 250 °C for 8 hours. Further analysis will be performed in search for a root-cause; but, it is clear that solderability of MetGlas™ is sensitive to solder composition. This finding certainly coincides with solderability differences exist between SnAgCu and SnAgBi on Cu substrates, whereby SnAgBi exhibits geneally lower contact angles for given temperatures and fluxes, [17, 18].

Referring to the meniscus height data for the exposed side, the values tended to be slightly larger for most of the 260 °C solder dips, indicating that a higher solder temperature improved the solderability of MetGlas™ base material. Both SnAgCu and SnAgBi produced similar, mean meniscus heights.

The data indicates that the MetGlas® fabrication process creates surfaces that can promote different solderability performances. It is unclear at this point whether it is a physical or chemical difference between them that is responsible for this observation. Morphological differences between the two surfaces may pose physical differences (roughness, thin oxide component, etc.) that impact wetting. Differences in atomic disorder, potentially generated by a temperature gradient can promote different chemical potentials for reacting with molten solder, hence changing the wettability reaction of the surface. A chemical contribution is likely responsible for an increased γ_{SL} and/or a decreased γ_{SL}, both of which decrease the driving force for the chemical reaction supporting wetting and spreading behavior. Since the SnAgBi meniscus heights didn't appear to change as the SnAgCu meniscus heights did, a solder alloy component has a significant effect that is synergistic with the physical and chemical variations to control wetting and spreading performance.

Figure 3-2 illustrates the maximum wetting force exerted by the solder menisci as a function of solder composition, solder temperature, and MetGlas™ aging condition. These data suggest that the SnAgCu solder exerts a larger wetting force in all scenarios compared to the SnAgBi solder. This is interesting since the SnAgCu didn't always travel farther upward along a given coupon, leading one to believe that it should exert the lesser force. Therefore, the shape of the solder meniscus exhibited less concavity for the SnAgCu alloy due to the different solder/flux surface tension. This finding illustrates the important premise that the meniscus height nor the meniscus weight should be used, alone, when a change in solder flux or composition occurs. Changes in solder flux and solder composition are likely accompanied by interfacial energy changes and reaction rate changes, which cannot be represented fully by either metric. Either metric should only be used to assess the solderability of like base materials using the same flux, solder composition, and solder temperature. Otherwise, solderability can only be accurately assessed by the contact angle.

Figure 3-2. Maximum force felt by a coupon for each solder composition, temperature, and aging condition.

3.2. Wetting Rate

Figure 3-3 shows the wetting rates for all sample sets. Note that because the wetting rate is obtained from the wetting curves, it is not possible to differentiate between coupon sides. Thus, the wetting rates represent the combined behavior between the two sides.

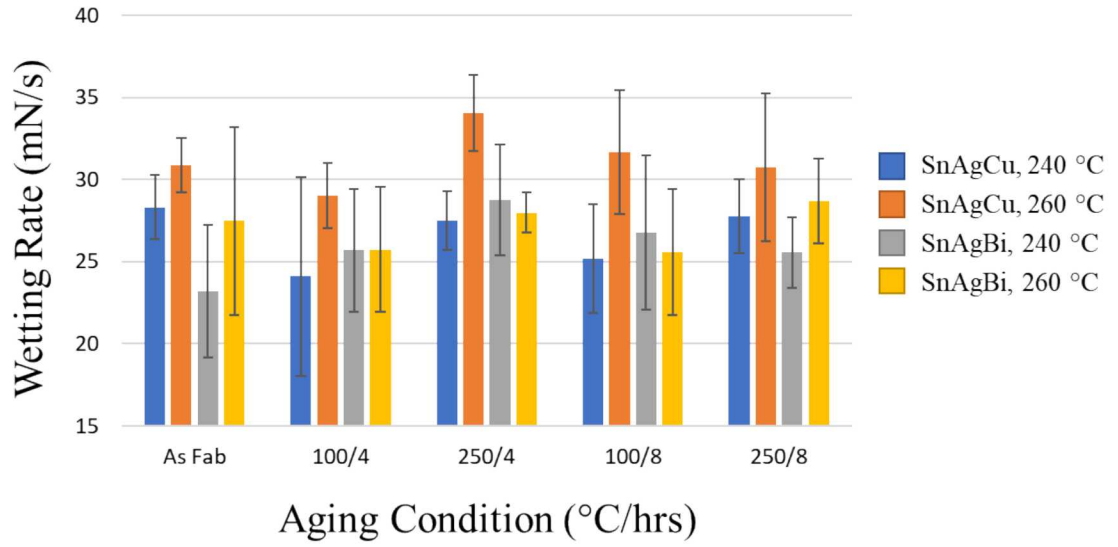

Figure 3-3. Wetting rates exhibited by both solders for the two test temperatures for all sample conditions.

The SnAgCu solder at 260 °C exhibits a higher *average* wetting rate than both its 240 °C counterpart and the SnAgBi solder at either temperature. The faster wetting rate of SnAgCu could be due to its increased chemical potential to dissolve and react with the base material, thereby more readily

forming an IMC layer. The wetting kinetics appear to be only temperature dependent for the SnAgCu solder. This might be due to the fact that SnAgBi solder has a lower melting temperature than SnAgCu and may be less sensitive to temperature changes in the studied range between 240 and 260 °C. At 240 °C, SnAgCu exhibits a wetting rate comparable to the SnAgBi solder. In contrast, the SnAgBi solder appears to wet at a rate that is independent of temperature. Although these scenarios were plausible, the reader is reminded that the wetting rates were not statistically different between nearly all cases in in Fig. 3-3.

Based upon the engineering perspective, less temperature dependence could provide the ability to produce more consistent solder joints due to a larger process window. The key point is that the interfacial energy relationship between solder, flux, and substrate changes when there is a change to any one of these factors. For example, one solder composition may have a temperature dependent interfacial chemical reaction, while another alloy exhibits an interfacial reaction rate independent of solder temperature.

3.3. Solder-Flux Interfacial Energy

Figure 3-4Figure 14 illustrates the solder-flux interfacial energy values for each coupon side.

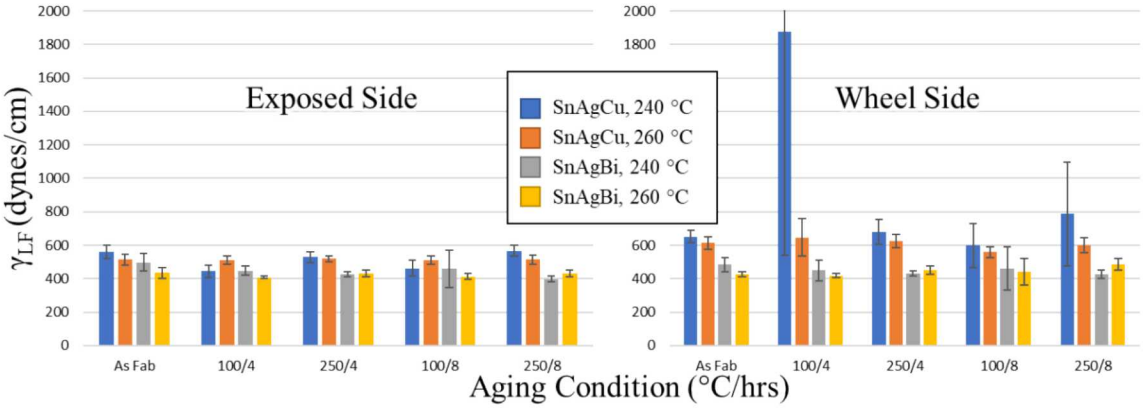

Figure 3-4. Solder-flux interfacial energy (γ_{LF}) values for each coupon side for all solder/temperature/aging condition combinations.

On both sides of the coupons, the SnAgBi solder exhibits a lower solder-flux interfacial energy than the SnAgCu solder, though the difference is much less on the exposed side compared to the wheel side. The lower the solder-flux interfacial energy, the greater is the propensity to wet. Again, it is possible that a temperature gradient during cooling produced different degrees of atomic disorder from side to side. Different atomic structure may influence the chemical potential of the substrate to dissolve and react with the molten solder. Substrate dissolution into liquid solder will further change the composition of the interface reaction zone and potentially, that of the liquid solder composition. The consequence is a change to the interfacial energy between the liquid solder and flux. The SnAgCu solder seems more sensitive to potentially different dissolution rates on the solder's interaction with the flux. The SnAgBi solder appears less sensitive to coupon side, indicating that different dissolution rates (i.e. slight composition changes) may not impact the molten solder composition and as such, the solder-flux interfacial tension.

The source of the extremely high interfacial energy for SnAgCu aged at 100 °C for 4 hours remains unknown. Work is ongoing to understand this outlier. One theory is that some process instability failed to produce atomic disorder in a small section of the MetGlas®.

Heat treatments do not appear to have a significant impact on either side, suggesting that any local atomic reordering is either minimal and/or does not intrinsically affect solderability.

3.4. Contact Angle

Contact angles for both the exposed and wheel sides are depicted in Figure 3-5.

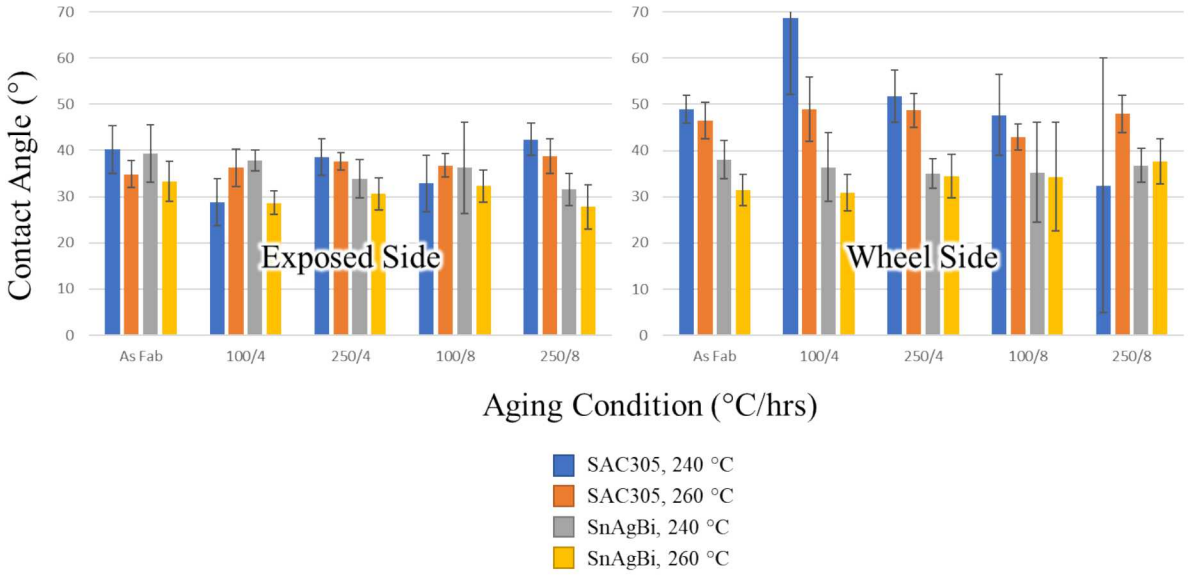

Figure 3-5. Contact angles for each coupon side for all solder/temperature/aging condition combinations.

Contact angles on the exposed side were generally lower and more tightly grouped (~30-40°) relative to the wheel side, where they were contained between 30 and 50°. The exception was the SnAgCu outlier that resulted in a relatively high contact angle near 70° noted above. An obvious correlation was absent between solder composition and contact angle on the exposed side. Aging also appeared to have little impact on contact angle. After the 250 °C aging, the SAC305 exhibits slightly larger values. However, the error bar overlap between data sets brings uncertainty into the significance of these trends. The higher solder pot temperature also tended to support lower contact angles, though again, the error overlap between data sets makes this less convincing.

The exposed side appears to be more viable to soldering operations, for both solder compositions. SnAgBi appears to exhibit better solderability on each side, relative to SnAgCu.

3.5. Force vs. Time Curves

Figure 3-6 to Figure 3-8 illustrate qualitative trends between the wetting curves for sample sets, further confirming that solder composition is the key variable that relates to solderability in this work, with negligible impact from solder temperature or coupon aging condition.

The aging does not appear to impact the solderability results in a statistically significant manner. Rather, the data suggests that either: 1) insufficient short-range order/crystallization took place to affect solderability or 2) the effects of any accompanying short-range order/crystallization does not intrinsically impact solderability. If reordering is minimal, the associated magnetic property degradation may also be negligible, suggesting that soldering may be an acceptable joining method.

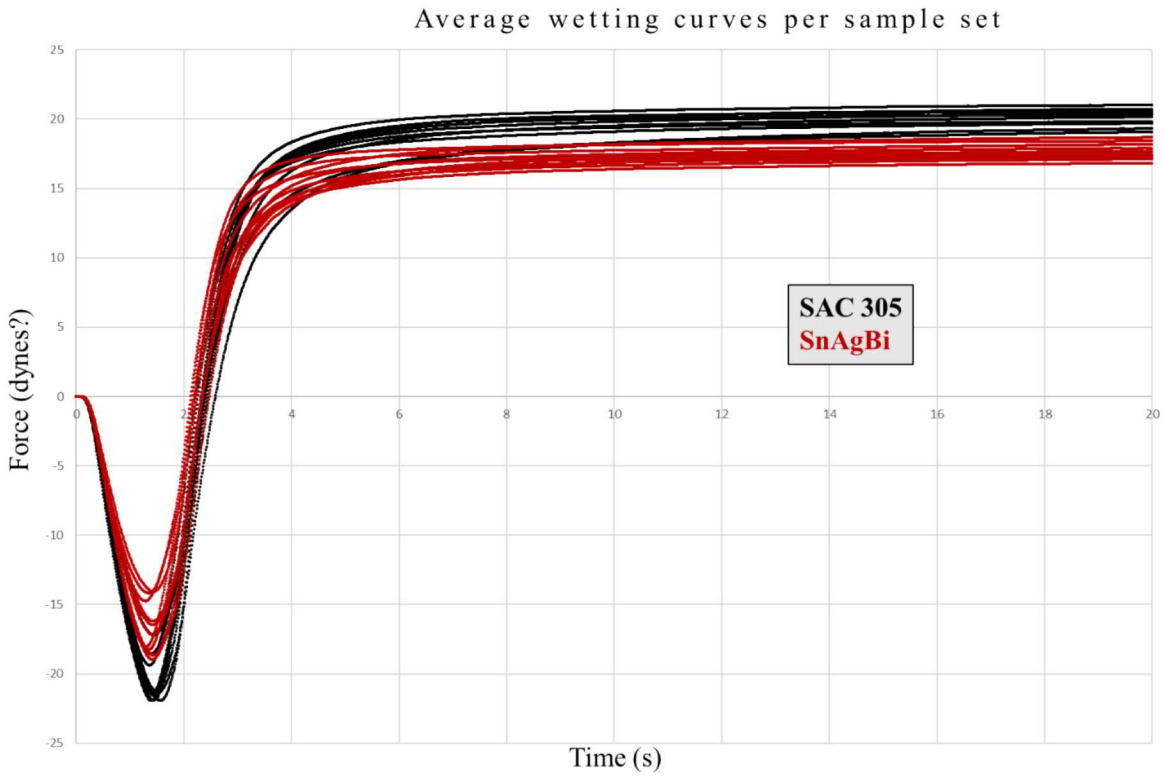

Figure 3-6. Average wetting curves taken for each sample set. Each line represents the averages of the 10 coupon dips per each unique combination of substrate given aging condition, solder composition, and solder temperature. This plot highlights all the sample sets dipped in SAC305 solder compared to those dipped in SnAgBi solder.

These wetting curves illustrate the solder composition dependency on wetting behavior. The coupons dipped in SnAgCu tend to experience a larger negative ("non-wetting") force prior to wetting and a larger maximum force after wetting occurs. Wetting rates for both liquid solders appear similar. The same data from Figure 3-6 is presented with respect to solder test temperature, and aging condition in Figure 3-7 and Figure 3-8, respectively.

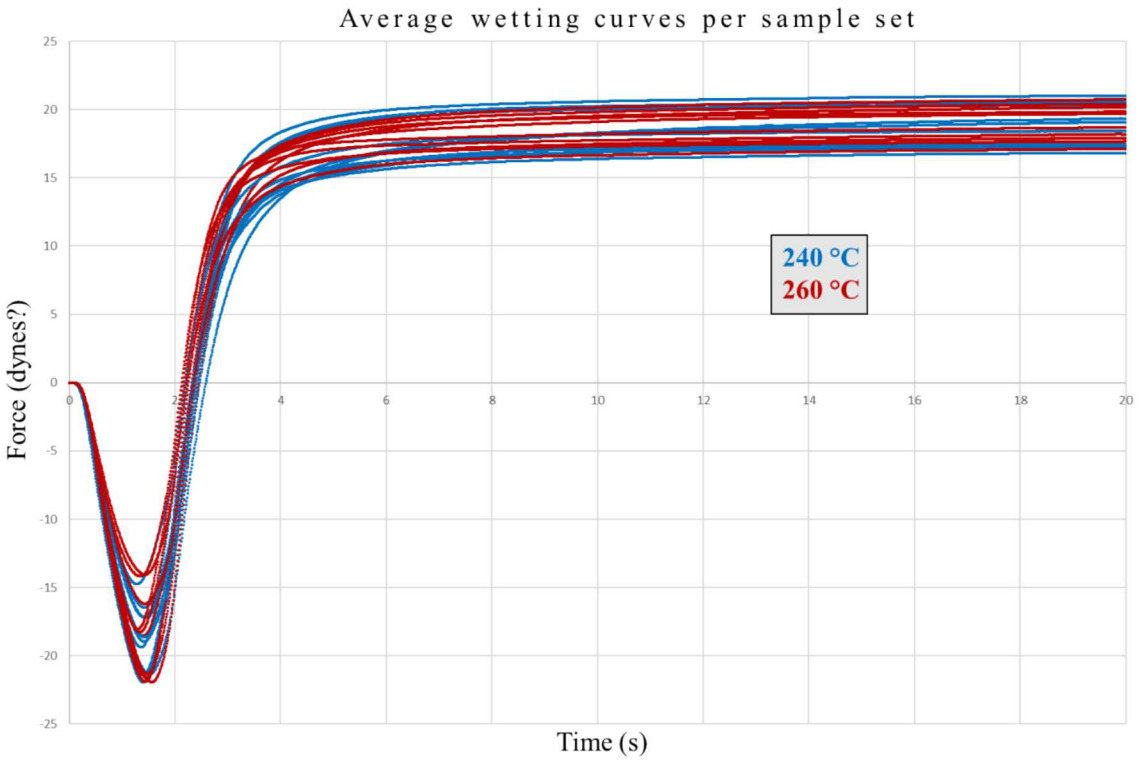

Figure 3-7. Average wetting curves taken for each sample set. Each line represents the averages of the 10 coupon dips per each unique combination of substrate given aging condition, solder composition, and solder temperature. This plot highlights samples dipped in 240 or 260 °C liquid solder.

No trends can be easily deduced from these curves, as curves from samples dipped in each temperature appear to overlap over the entire range of data.

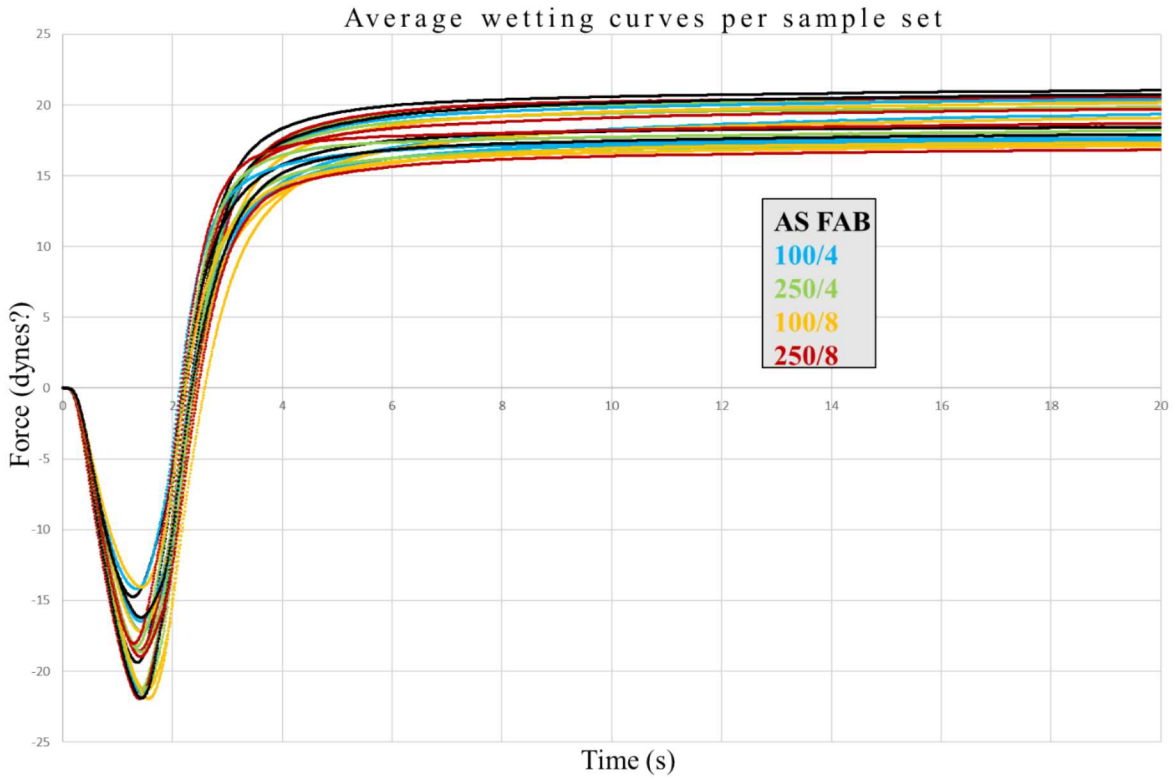

Figure 3-8. Average wetting curves taken for each sample set. Each line represents the averages of the 10 coupon dips per each unique combination of substrate given aging condition, solder composition, and solder temperature. This plot highlights the aging conditions that substrates were subjected to prior to dipping.

Significant trends did not emerge with respect to wetting curve as a function of MetGlas™ coupon aging treatment. The important finding, which was obtained from the wetting curves in Figure 16 to Figure 18 , is that when considering the variables of solder composition, solder temperature, and substrate aging condition, the solder composition has the greatest effect. Any changes to surface atomic structure, which were initiated by the aging treatments, were either intrinsically negligible to solderability or if present, were overwhelmed by solder composition effects.

3.6. Solder Assessment

Finally, the quality of the solder coating on the MetGlas substrates was assessed, visually. Figure 3-9 shows how many coupons in a sample set exhibited solder dewetting. Each sample set consisted of 10 coupon dips, so 10 dewetting instances means that all 10 coupons had portions of visibly dewet regions.

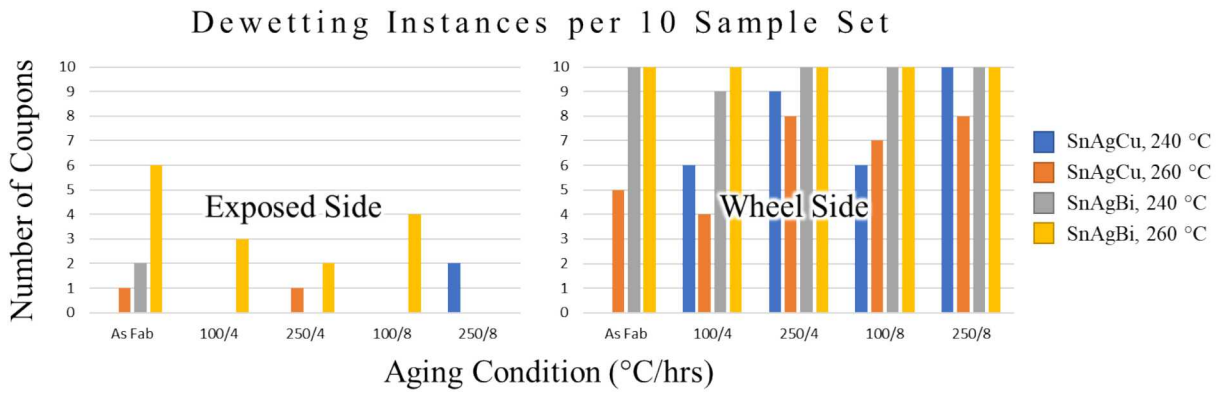

Figure 3-9. Number of samples that exhibited solder dewetting per sample set on each coupon side as per aging and solder/solder temperature variations. Each sample set contained 10 samples.

The wheel side of each MetGlas™ coupon experienced significantly more dewetting than did the exposed side, regardless of solder composition, solder temperature, or aging condition. The coupons dipped in SnAgBi solder appeared to dewet more often than those dipped in SnAgCu. Coupons dipped in the hotter SnAgCu solder exhibited less dewetting than those dipped in the cooler SnAgCu. The coupons aged at 250 °C exhibited the most dewetting, suggesting that aging did impact wetting behavior though not evident from the solderability test data.

A possible explanation for the extreme dewetting on the wheel side, relative to the exposed side, again, might point toward different dissolution tendencies between the sides, driven by a possible cooling rate dependent microstructure of the amorphous metal. Dissolution rates may be locally inconsistent, if the atomic disorder is also locally varied. The interfacial reaction necessary for wetting, may be spatially inconsistent, occurring in some areas and not others, hence resulting in dewetting.

The quantitative solderability data did not show dramatic differences between coupon sides. However, those data represent the global solderability performance of the coupons. The dewetting behavior provides evidence that the surface conditions on a local scale establish a level of dependency of solderability on the structural relaxation by MetGlas® substrates.

4. CONCLUSION

This study examined the solderability performance of two Pb-free solders on a rapidly solidified metallic glass foil base material. The long-term objective of this work was to establish a knowledge base for the potential use of lower-temperature, filler metal joining technology with temperature sensitive, rapidly solidified materials. Specifically, this study explored the molten solder, wetting and spreading performance on the surfaces of non-equilibrium, solidified structures. These findings can be applied towards developing a fundamental understanding of the interface reactions between molten solder and other, non-equilibrium materials – e.g., additively manufactured (AM) copper components – as an avenue towards developing suitable joining technologies.

The main findings are reported below:

1. MetGlas™ solderability ranged from "good" to "very good" on the exposed side and "good" to adequate" on the wheel side, based on contact angle calculations. Soldering applications should aim to exploit the more solderable, exposed side, when possible.
2. Solder composition was the most dominant factor on solderability trends, indicating that solder selection will likely be key for producing the best joints. Solder temperature and aging condition were less impactful regarding solderability behavior, which indicates that structural relaxation (atomic reordering)/recrystallization was not activated at solder temperatures and that structural relaxation and/or recrystallization prior to the soldering process, had a negligible effect on solderability. Of course, higher soldering temperatures may support a different metallurgical bond at the interface that, in turn would alter solderability performance.
3. Both the exposed and wheel sides supported similar meniscus heights, but dewetting occurred much more regularly on the wheel sides. A difference in cooling conditions may have produced slightly different, localized atomic (ordering) structures on the two sides, thus influencing substrate dissolution rates on that scale.

REFERENCES

[1] Humpston, G. and D.M. Jacobson, *Principles of Soldering*. 2004, Materials Park, Ohio: ASM International.

[2] Manko, H.H., *Solders and Soldering: Materials, Design, Production, and Analysis for Reliable Bonding*. 4th ed. 2001, New York: McGraw-Hill.

[3] EIA/IPC/JEDEC, *J-STD-002E: Solderability Tests for Component Leads, Terminations, Lugs, Terminals, Wires*. 2017.

[4] IPC, *IPC J-STD-003C: Solderability Tests for Printed Boards*. 2013, IPC.

[5] (EIA), E.I.A., *EIA/IS-86: Surface Mount Solderability*. 1993, EIA.

[6] Xu, F., R. Farrell, and R. Mohanty, *To Quantify a Wetting Balance Curve*. Enthone Inc.

[7] Wassink, R.J.K., *Soldering in Electronics: A Comprehensive Treatise on Soldering Technology for Surface Mounting and Through-Hole Techniques*. 2nd ed. 1989, Ayr, Scotland: Electrochemical Publications.

[8] Thwaites, C.J., *Solderability and Some Factors Affecting it*. Brazing and Soldering, 1981. **1**(3): p. 15-18.

[9] Vianco, P., *Soldering Handbook*. 3rd ed. 1999, Miami: American Welding Society.

[10] Gunter, I.A. and D.M. Jacobson, *The GEC Meniscograph Solderability Tester: Adaptation to Vacuum Soldering*. GEC REv., 1990. **6**(2): p. 86-89.

[11] Matienzo, L.J. and R.R. Schaffer, *Wetting Behaviour of Eutectic Tin/Lead Solder and Fluxes on Copper Surfaces*. Journal of Material Science, 1991. **26**: p. 787-791.

[12] Vianco, P.T., F.M. Hosking, and J.A. Rejent, *Wettability of Metallic Glass Alloys by Two Tin-Based Solders*. Welding Journal, 1994.

[13] Tormes, C.D., et al., *Characterization of Drying Behavior of Granular Materials Using Magnetoelastic Sensors*. NDT & E International, 2014. **66**: p. 67-71.

[14] Mayhew, A.J. and G.R. Wicks. *Solderability and Contact Angle*. in *Proceeding INternational Nepcon III*. 1971.

[15] Vianco, P., *Understanding the Reliability of Solder Joints Used in Advanced Structural and Electronics Applications: Part 2-Reliability Performance*. Welding Journal Supplement, 2017. **96**: p. 83-94.

[16] Vianco, P., *Understanding the Reliability of Solder Joints used in Advanced Structural and Electronics Applications: Pat 1- Filler Metal Properties and the Soldering Process*. Welding Journal Supplement, 2017. **96**: p. 39-52s.

[17] Lopez, E.P., P.T. Vianco, and J.A. Rejent, *Solderability Testing of 95.5Sn-3.9Ag-0.6Cu Solder on Oxygen-Free High-Conductivity Copper and Au-Ni-Plated Kovar*. J. of Electronic Materials, 2003. **32**(4): p. 254-260.

[18] Vianco, P.T. and J.A. Rejent, *Properties of Ternary SnAgBi Solder Alloys: Part II- Wettability and Mechanical Properties Analyses*. J. of Electronic Materials, 1999. **28**(10).

APPENDIX A. CALCULATING SOLDER-FLUX INTERFACIAL ENERGY, CONTACT ANGLE, AND TILT ANGLE VALUES FROM MENISCUS HEIGHT (H) AND WEIGHT (W)

Adapted from discussions and schematics presented by Vianco et al.[1] and Mayhew and Monger[2].

A.1. Solder-Flux Interfacial Energy (γ_{LF})

The meniscus weight, W, is used to determine the solder-flux interfacial energy, γ_{LF}. Equation 1 shows the formula for meniscus weight.

$$W = \rho g P A \quad (1)$$

ϱ = solder density
g = acceleration due to gravity
P = sample perimeter
A = cross-sectional area of meniscus profile

While ϱ, g, and P are straight-forward, the cross-sectional area, A, of the meniscus profile requires integrating the meniscus profile (to calculate area under the profile curve). As such, an expression for the meniscus surface profile is first required:

$$A = \int_0^H x(y)dy \quad (2)$$

H = meniscus height
x(y) = expression describing meniscus surface profile

Therefore:

$$W = \rho g P \int_0^H x(y)dy \quad (3)$$

A schematic illustrating the dipping scenario is provided below in Figure A-1, where liquid has wet the coupon, risen to height, H, and contacted the coupon at an angle, θ_C. Equations 4-11.2 show how x(y) can be derived.

[1] Vianco, P.T., F.M. Hosking, and J.A. Rejent, Wettability of Metallic Glass Alloys by Two Tin-Based Solders. Welding Journal, 1994.
[2] A. Mayhew and K. Monger, *Proc. Inter.* NEPCON (1972)

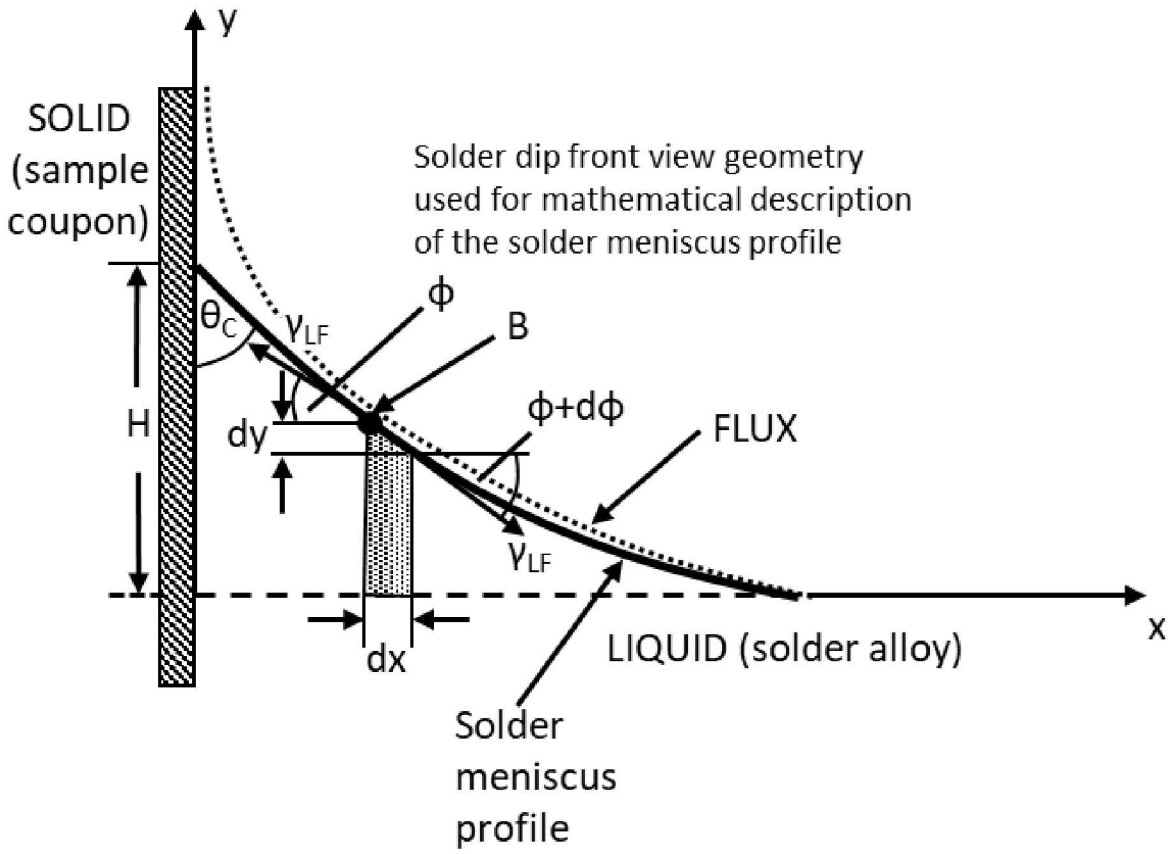

Figure A-1. Schematic of liquid wetting a coupon dipped into molten solder.

To derive an expression for the solder meniscus profile, consider the equilibrium forces acting on point B. The weight of the solder exerts a downward force, but an equal and opposite force is realized due to the force at the liquid-flux interface. Since the flux extends to the surface of the liquid solder, both a downward and an upward force are felt. The difference of these forces must equal the downward gravitational force. Applying this equilibrium force relationship to a differential slice of solder produces Equation 4 (if the solder-flux interfacial energy is the only source for solder wetting):

$$\gamma_{LF}\sin\varphi - \gamma_{LF}\sin(\varphi + d\varphi) - \rho g y dx = 0 \quad (4)$$

$$\gamma_{LF}\sin\varphi - \gamma_{LF}\sin(\varphi + d\varphi) = \rho g y dx$$

Since:

$$\gamma_{LF}\sin\varphi - \gamma_{LF}\sin(\varphi + d\varphi) \approx \gamma_{LF} d(\sin\varphi)$$

Then equation 4 simplifies to:

$$\gamma_{LF} d(\sin\varphi) = \rho g y dx \quad (4.1)$$

Rearrange equation 4.1:

$$\frac{d(\sin\varphi)}{dx} = \frac{\rho g y}{\gamma_{LF}} \tag{4.2}$$

Since:

$$\frac{d(\sin\varphi)}{dx} = -\frac{d(\cos\varphi)}{dy} \tag{5}$$

Therefore:

$$-\frac{d(\cos\varphi)}{dy} = \frac{\rho g y}{\gamma_{LF}} \tag{4.3}$$

Integrating from 0 to φ:

$$1 - \cos\varphi = \frac{\rho g y^2}{2\gamma_{LF}} \tag{4.4}$$

Consider the location where the solder contacts the plate:

$$y = H; \quad \varphi = 90° - \theta_C$$

Therefore:

$$\cos\varphi = \sin\theta_C \tag{6}$$

Hence: Integrating Equation 4.4 results in an expression that relates the contact angle to meniscus height, density, and solder-flux interfacial energy:

$$\boxed{1 - \sin\theta_C = \frac{\rho g H^2}{2\gamma_{LF}}} \tag{7}$$

θ_C = contact angle
H = meniscus height

Consider a very specific circumstance. For perfect wetting, $\theta_C = 0°$ and y = Y. Therefore:

$$\gamma_{LF} = \frac{1}{2}\rho g Y^2 \tag{7.1}$$

And when substituted into the previous equation:

$$1 - \sin\theta_C = \frac{y^2}{Y^2} \tag{7.2}$$

Allows for the calculation of y/Y, which is necessary to plot a meniscus profile (x/y vs. y/Y)

To relate the interfacial energy to measurable quantities, consider the equilibrium of the surface to the left of point B (in original diagram) and resolve vertically. The weight of the column of liquid must be supported. Substituting equations 8 (from geometric consideration of the initial schematic) and 7.2, rearrange and integrate equation 4.4:

$$\gamma_{LF}(1 - \cos\theta_C) = \int_y^Y \rho g y dx \tag{4.4}$$

$$dx = -dy\tan\theta_C; 1 - \sin\theta_C = \frac{y^2}{Y^2}$$

For geometry relations: (8; 7.2)

$$2ydy = -Y^2\cos\theta_C d\theta_C \quad (9)$$

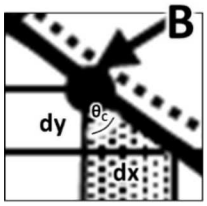

$$dx = \frac{Y\sin\theta_C\, d\theta_C}{2\sqrt{(1-\sin\theta_C)}}$$

Now, let $q^2 = 1 + \sin\theta_C$, therefore:

$$\sin\theta_C = q^2 - 1 \text{ and } 1 - \sin\theta_C = 2 - q^2 \quad (10, 10.1)$$

Apply some crafty math using equations 10 and 10.1:

$$2qdq = \cos\theta d\theta = \sqrt{(1-sin^2\theta)}d\theta = q\sqrt{(2-q^2)}d\theta \quad (10.2)$$

Substitute into equation 9:

$$dx = \frac{Y}{2}\frac{q^2-1}{\sqrt{(2-q^2)}}\frac{2dq}{\sqrt{(2-q^2)}} \quad (11)$$

$$dx = Y\frac{q^2-1}{2-q^2}dq$$

Integrate with following limits:
θ from 0 (perfect wetting) to 90° (no wetting)
q from 1 to √2

$$x = Y\int_1^q \frac{q^2-1}{2-q^2}dq = Y\int_1^q \left(\frac{1}{2-q^2}-1\right)dq = Y\int_1^q \frac{1}{2\sqrt{2}}\left(\frac{dq}{\sqrt{2}-q}+\frac{dq}{\sqrt{2}+q}\right)-dq = Y\left[\frac{1}{2\sqrt{2}}lo\right.$$

Finally, an expression that describes the meniscus surface profile coordinates [x(y), y]: (11.1)

$$x(y) = \sqrt{\frac{2\gamma_{LF}}{\rho g}}\left\{\frac{1}{2\sqrt{2}}\,ln\left[\frac{\sqrt{2}+q}{\sqrt{2}-q}\right]-\frac{1}{2\sqrt{2}}ln\left[\frac{\sqrt{2}+q_c}{\sqrt{2}-q_c}\right]-q+q_c\right\}$$

Where: (11.2)

$$q = \sqrt{(2-\frac{\rho g y^2}{2\gamma_{LF}}} \text{ and } q_c = \sqrt{(2-\frac{\rho g H^2}{2\gamma_{LF}}} \quad (12, 12.1)$$

After substituting equations 12 and 12.1 into equation 11.2, the cross-sectional area becomes:

$$A = \frac{H}{2}\sqrt{\left(\frac{4\gamma_{LF}}{\rho g}\right)-H^2} \quad (13)$$

And substituting equation 13 into equation 1 leads to:

$$W = \rho g P \frac{H}{2}\sqrt{\left(\frac{4\gamma_{LF}}{\rho g}\right) - H^2} \tag{14}$$

Mayhew and Monger apply limits to this equation to solve for x/Y, to solve for y/Y for a given θ to construct the meniscus profile. Their paper provides excellent details.
And, because W and H are experimental measurements, this expression can be rearranged and solved for γ_{LF}:

$$\boxed{\gamma_{LF} = \frac{\rho g}{4}\left[\frac{4W^2}{(\rho g P H)^2}\right] + H^2} \tag{14.1}$$

A.2. Contact Angle (θ_C)

Plug equation 14 into the integration of the force balance equation (eqn 2):

$$\boxed{\theta_C = \sin^{-1}\left[\frac{4W^2 - (\rho g P H^2)^2}{4W^2 + (\rho g P H^2)^2}\right]} \tag{15}$$

The θ_C and γ_{LF} values can then be input into Young's equation to calculate (γ_{SF} - γ_{SL}).

**Note: The above derivation assumes that the solder meniscus rises evenly on all 4 faces, but this is not the case due to implications from the corners and the fluid nature of the solder. The above derivation also neglects buoyancy force (BF). To account for buoyancy, subtract BF from the W. Most automated wetting balances account for BF. For more detailed information refer to Vianco et al. (I think source 10?).

A.3. Tilt Angle (δ)

The above derivation also assumes that all 4 surfaces produce equivalent wetting. This may not always be the case depending on sample processing conditions. One side may also be coated. The derivation for a tilt angle caused by asymmetric wetting is shown below in Figure A-2.

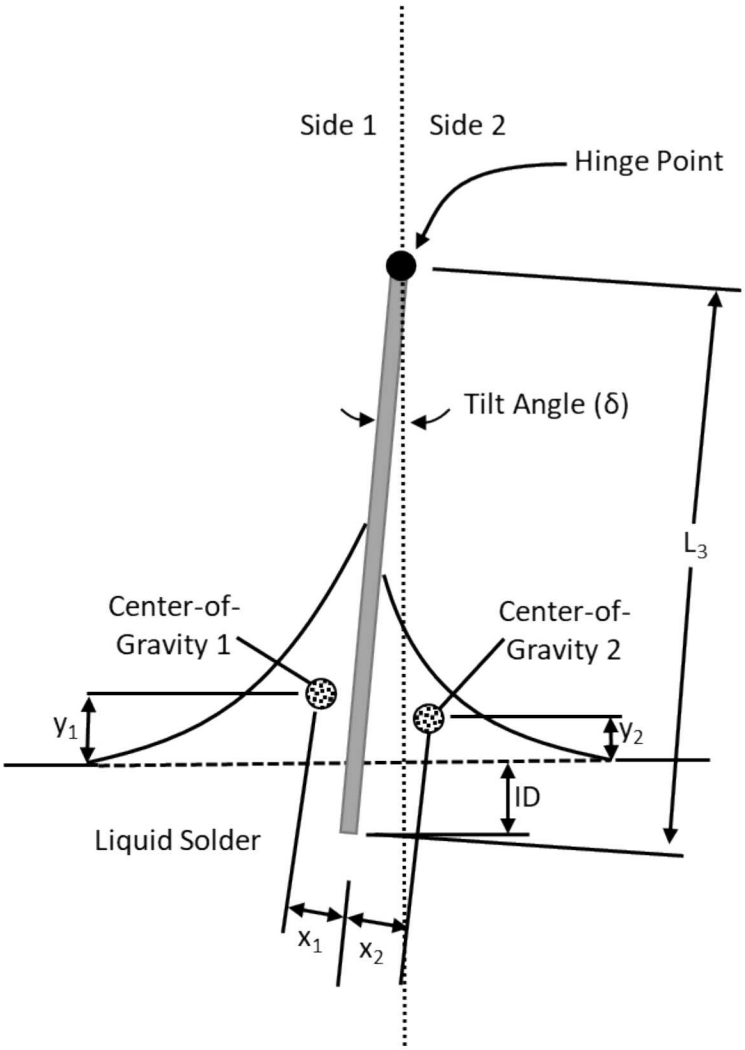

Figure A-2. Schematic of tilted coupon due to different wettability on each side.

In this instance the scenario is broken into two halves because contact angles on both sides of the coupon must be determined. The total meniscus weight is therefore characterized as the sum of the meniscus weights from either side.

$$W = W_1 + W_2 \tag{16}$$

Where W_i (i=1,2) are given as:

$$W_i = \rho g \frac{PH}{2\,2} \sqrt{\frac{4\gamma_{LF}}{\rho g} - H_i^2} \tag{17}$$

Substituting equation 17 into equation 16 gives:

$$W = \frac{\rho g P}{4}\left[H_1\sqrt{\frac{4\gamma_{LF}}{\rho g} - H_1^2} + H_2\sqrt{\frac{4\gamma_{LF}}{\rho g} - H_2^2}\right] \tag{16.1}$$

The above eqn__ can be solved transcendentally for γ_{LF}, and contact angles for both sides ($\theta_{C,1}$ and $\theta_{C,2}$) can be calculated with equation 15 (for each coupon half).

$$1 - \sin\theta_{C,i} = \frac{\rho g H_i^2}{2\gamma_{LF}} \tag{15}$$

A torque will be generated by the different menisci, allowing a tilt angle to be approximated from geometrical relationships between the centers-of-gravity (CGs) for each meniscus. The x coordinates of the CGs were calculated from (where $k=g/4\gamma_{LF}$):

$$\bar{x}_i = \frac{1}{2A_i}\int_0^H [x_i(y)]^2 dy \tag{18}$$

$$\bar{x}_i = \frac{1}{4kA_i}\left\{\frac{1}{\sqrt{k}}\left[\frac{1}{2}ln\left(\frac{1+\sqrt{\left(1-kH_i^2\right)}}{1-\sqrt{\left(1-kH_i^2\right)}}\right) - \sqrt{\left(1-kH_i^2\right)}\right]\left[\sin^{-1}\sqrt{\left(1-kH_i^2\right)} + \sin^{-1}\sqrt{k}H_i\right.\right.$$

The y-coordinates can be similarly calculated:

$$\bar{y}_i = \frac{1}{3kH_i}\left\{kH_i^2 - \frac{1}{2\sqrt{\left(1-kH_i^2\right)}} + \frac{1}{2}\right\} \tag{19}$$

Finally, the tilt angle, δ, can be determined:

$$\delta = \tan^{-1}\left\{\frac{W_2\bar{x}_2 - W_1\bar{x}_1}{(L_3 - ID)(W_1 + W_2) - W_1\bar{y}_1 - W_2\bar{y}_2}\right\} \tag{20}$$

DISTRIBUTION

Email—Internal

Name	Org.	Sandia Email Address
Rebecca Wheeling	1831	rwheeli@sandia.gov
Paul Vianco	1831	ptvianc@sandia.gov
Shelley Williams	1831	shewill@sandia.gov
Collin Donohoue	1831	cddonoh@sandia.gov
Cole Yarrington	1851	cdyarri@sandia.gov
Technical Library	01977	sanddocs@sandia.gov

Hardcopy—Internal

Number of Copies	Name	Org.	Mailstop
2	Rebecca Wheeling	1831	0889

This page left blank

This page left blank

Sandia National Laboratories

Sandia National Laboratories is a multimission laboratory managed and operated by National Technology & Engineering Solutions of Sandia LLC, a wholly owned subsidiary of Honeywell International Inc. for the U.S. Department of Energy's National Nuclear Security Administration under contract DE-NA0003525.